Geophysical Research Letters

RESEARCH LETTER
10.1029/2019GL085363

Significant Spatial Variability in Radar-Derived West Antarctic Accumulation Linked to Surface Winds and Topography

Marissa E. Dattler[1,2,3], Jan T. M. Lenaerts[1], and Brooke Medley[3]

[1]Department of Atmospheric and Oceanic Sciences, University of Colorado Boulder, Boulder, CO, USA, [2]Department of Atmospheric and Oceanic Sciences, University of Maryland, College Park, MD, USA, [3]Cryospheric Sciences Laboratory, NASA Goddard Space Flight Center, Greenbelt, MD, USA

Key Points:
- We compute spatial variations in accumulation from along-track fluctuations in radar-derived firn layer depth
- Our rates are forced by reanalysis on a 25-km scale but reveal significant variability on smaller scales, with regional dependence
- Areas with strong variations in topographic surface slope in the near-surface wind direction correlate with high accumulation variability

Supporting Information:
- Supporting Information S1

Correspondence to:
M. E. Dattler,
marissadattler@gmail.com

Citation:
Dattler, M. E., Lenaerts, J. T. M., & Medley, B. (2019). Significant spatial variability in radar-derived West Antarctic accumulation linked to surface winds and topography. *Geophysical Research Letters*, *46*, 13,126–13,134. https://doi.org/10.1029/2019GL085363

Received 10 SEP 2019
Accepted 12 NOV 2019
Accepted article online 15 NOV 2019
Published online 25 NOV 2019

Abstract Across the Antarctic Ice Sheet, accumulation heavily influences firn compaction and surface height changes. Therefore, accumulation varies over short distances (<25 km), complicating the derivation of ice sheet mass changes from altimetry and reducing how accurately field measurements can be spatially extrapolated. However, current atmospheric reanalyses have grid spacings (>25 km) that are too coarse to resolve this variability. To address this limitation, we construct a fine-scale accumulation product from airborne snow radar observations by superimposing along-track fluctuations in accumulation onto an atmospheric reanalysis product. Our resulting airborne product reflects large-scale (>25 km) orographic precipitation patterns while providing robust and unprecedented insight into Antarctic accumulation variability on subgrid scales. On these smaller scales, we find significant, regionally dependent accumulation variability ($\sigma_{relative} > 40\%$). This variability in accumulation is correlated with variability in topographic surface slope in the wind direction ($p < 0.01$), confirming that subgrid-scale accumulation variability is driven by snow redistribution by wind.

Plain Language Summary Satellite altimetry observations measure how the surface height of the Antarctic Ice Sheet is evolving. To understand the drivers of surface height changes, we must determine how much snow is accumulating onto the surface and how fast deeper snow is compacting under the weight of new snow accumulation. Therefore, scientists need to compute accumulation rates across the surface of the ice sheet to estimate ice mass loss and sea level rise from satellite data. In this study, we calculate snow accumulation rates over a significant portion of the Antarctic Ice Sheet from an airborne radar instrument. On length scales shorter than 25 km, this product reveals variations in snow accumulation that result from the strong winds over Antarctica interacting with surface topography. Wind transports snow from the ice sheet's surface and deposits it downwind, leading to reduced accumulation in regions of erosion and greater accumulation in regions of deposition. This relationship is reflected in our accumulation product; regions of high spatial variability in accumulation tend to also have high variability in wind speed, wind direction, and ice sheet surface topography. Our work constitutes substantial progress towards calculating accumulation at small spatial scales over ice sheets.

1. Introduction

Since 1979, the West Antarctic Ice Sheet (WAIS) and the Antarctic Peninsula Ice Sheet (APIS) have contributed 6.9 ± 0.6 and 2.5 ± 0.4 mm to global sea level change (GSLC), respectively (Rignot et al., 2019). A grounded ice sheet's impact on GSLC is determined by its mass balance or the difference between accumulation onto its surface and flux of ice across its grounding line (Shepherd et al., 2018). Therefore, if we are able to better constrain accumulation over the WAIS and APIS, we can reduce uncertainty in their contributions to GSLC.

Over the WAIS and APIS, virtually all surface meltwater refreezes in place and meltwater runoff is negligible (e.g., Kuipers Munneke et al., 2012; Lenaerts et al., 2012; Trusel et al., 2013). Therefore, we are able to approximate accumulation over these two ice sheets as precipitation minus evaporation, $P - E$. Evaporation is almost entirely comprised of sublimation since nearly all liquid water produced at the surface of the WAIS and APIS instantaneously percolates and refreezes (Trusel et al., 2013).

Current atmospheric reanalysis products, such as Modern-Era Retrospective Analysis for Research and Applications (MERRA-2) and European Centre for Medium-Range Weather Forecasts Interim ReAnalysis (ERA-Interim), are able to resolve variations in Antarctic accumulation rates on horizontal length scales that are equal to or larger than their grid sizes (~50–100 km), which are largely driven by orographic precipitation gradients (Gelaro et al., 2017; Medley et al., 2013; Nicolas & Bromwich, 2011; Palerme et al., 2017; van den Broeke et al., 2006). Compared to Antarctic ice core observations, MERRA-2 shows the lowest bias in large-scale accumulation among reanalysis products (Medley & Thomas, 2019).

However, all reanalysis products fail to resolve smaller-scale, wind-driven redistribution of snow (Lenaerts et al., 2012). Wind-driven redistribution of snow can cause spatial variability in accumulation on subgrid scales (<25 km; Liston & Sturm, 1998). This is especially true in the windy and dry interior regions of the Antarctic Ice Sheet (AIS; Eisen et al., 2008). Snow redistribution originates from small-scale topographic variations (5–25 m in height) on the surface that are unresolved by the coarse spatial grids of reanalysis products. Snow is scoured from windward topographical slopes and redeposited downwind, resulting in spatially variable accumulation (Arcone et al., 2012; Fahnestock et al., 2000; Frezzotti et al., 2002; Hawley et al., 2014).

These spatial variations in accumulation have direct implications for ice core and altimetry studies. Since ice cores are point measurements, one must consider local spatial variability in accumulation when extrapolating their observations over large areas. Accumulation rates at fine spatiotemporal resolution are also necessary for estimating temporal changes in firn compaction. Accurately modeling these firn compaction rates across the AIS is necessary to derive mass change from temporal changes in surface elevation measured by laser or radar altimetry (e.g., Sandberg Sørensen et al., 2011; Shepherd et al., 2018; Zwally et al., 2015). Small-scale spatial variations in accumulation are not resolved in these estimates of mass change; models of firn compaction are typically forced by data from regional climate models or reanalyses, whose resolutions are too coarse to account for the effects of snow redistribution by wind. An accumulation product that can match the resolution of current altimetry measurements (<5 km) would allow for more accurate estimates of mass change from surface height changes (Csatho et al., 2019).

The National Aeronautics and Space Administration Operation IceBridge (OIB) snow radar is a promising tool to capture small-scale variations in accumulation as it is able to track internal stratigraphy with an along-track sampling frequency of one trace per every 5 to 10 m. The airborne OIB campaigns have been collecting observations over large portions of the WAIS and APIS annually for the past decade (2009–2019). Up until present, analysis of OIB snow radar derived accumulation rates over the AIS has been limited to the middle-to-upper Thwaites and Pine Island glacier catchments (Medley et al., 2013, 2014), coastal ice domes (Lenaerts et al., 2017), and the Larsen C ice shelf (Kuipers Munneke et al., 2017).

In this study, we present a new snow accumulation product that represents a much more expansive area than that of previous studies. In addition to Thwaites and Pine Island glacier catchments, our product provides coverage of most of coastal West Antarctica and parts of the APIS, Ronne Ice Shelf, and South Pole region. The total length covered by all of our flight lines (17,500 km) is over seven times that of the most extensive previous study of snow radar-derived accumulation over the AIS (Medley et al., 2013).

In order to achieve this degree of coverage, we created an algorithm that is unique in its independence from ice cores and other in situ information. This independence allows us to apply the algorithm to snow radar observations covering any region of the AIS, regardless of its proximity to ice cores. To circumvent the need for external input, we initially assume that $P - E$ from MERRA-2 is accurate for length scales over 25 km, as it performs best among other reanalysis products (Medley & Thomas, 2019). We then generate an accumulation product that reflects this reanalysis product, including all of its errors, on scales over 25 km. However, our accumulation product also resolves smaller-scale variations that we derive from snow radar data. To analyze these small-scale spatial variations in accumulation, we focus on a relative accumulation product that both reflects the subgrid-scale accumulation variation and is shown to be largely independent of MERRA-2's absolute accumulation field. In our analysis, we correlate variations in relative accumulation to variations in topography, wind speed, and wind direction. Lastly, we discuss the implications of these relationships on calculating accumulation over regions of the WAIS and APIS not surveyed by the airborne radar.

2. Methods

2.1. Absolute Radar-Derived Accumulation Rates

We estimate accumulation rates with unprecedented coverage of the WAIS and APIS at 100-m along-track spacing from 29 OIB snow radar flights between 2010 and 2017. We focus this analysis on along-track gradients in accumulation and on their regional variations. Therefore, we pick a subset of 29 surveys that spatially covers a large portion of these two ice sheets. Additionally, we exclude flight lines with heavily discontinuous internal reflection horizons (IRHs). These discontinuities result from either (a) rapid changes in aircraft altitude in response to steep surface topography or (b) disruptions in firn stratigraphy caused by reworking of the snow at the surface in low accumulation conditions. Given our data subselection and quality control, we create an expansive product that includes 175,373 individual accumulation measurements.

IRHs within the snow and firn are interpreted as isochrones (i.e., representative of a single time or event); therefore, the mass between horizons (cumulative mass) can be used to calculate accumulation rates (Eisen et al., 2005; MacGregor et al., 2009; Medley et al., 2013, 2014, 2015; Sinisalo et al., 2003). In this study, we calculate accumulation rates from snow radar data using two isochrones: the surface and a single IRH.

We divide the snow radar data into 25-km along-track segments, tracking the surface and a continuous and clearly resolved IRH within the first 50 m of snow and firn. We use semiautomated layer picking software to track these horizons, visually verifying and manually retracking as necessary. Our software produces one layer pick per 100 m along track. To obtain a greater signal to noise ratio, we preferentially select deeper (closer to 50 m) IRHs wherever possible, as a horizon's along-track variation tends to amplify with depth.

By tracking the clearest IRH within the first 50 m of snow and firn, we average accumulation over multiple years. For each segment, this time span depends on the accumulation rate, depth of the tracked IRH, and the year of the OIB overflight. Although this methodology results in time spans that vary from segment to segment, tracking the clearest IRHs reduces uncertainty in layer picking. Moreover, we assume that spatial variations in accumulation are persistent in time for length scales between 100 m and 25 km (Medley et al., 2013). Given this assumption, we are able to track the best-resolved IRHs to quantify spatial variability in accumulation by averaging over multiple years.

To calculate accumulation rates, we first compute cumulative mass, or the integral of density with depth, between two horizons. At every 100 m along track, we record the two-way travel time (TWTT) between the surface and the IRH for a total of 250 layer picks per 25-km flight segment. At each of these 100-m-spaced layer picks, we generate a depth-density profile using a semiempirical, steady-state firn compaction model (Herron & Langway, 1980). We use mean $P - E$ and 2-m air temperature from MERRA-2, in addition to initial snow density of 350 kg/m^{-3} based on ice core observations (see supporting information Figure S1), as input into this model. By calculating the depth-permittivity profile from the modeled depth-density profile (Kovacs et al., 1995), we are able to convert TWTT to depth. We integrate the depth-density profile from the IRH to the surface at each layer pick to find cumulative masses that vary from pick to pick along the segment. This method of calculating cumulative mass is described in detail in Medley et al. (2015).

In this ice sheet-wide study, we determine the age of an IRH using a methodology that differs from previous, region-specific studies (e.g., Medley et al., 2013, 2015), in which a layer's age was determined either from ice cores or by counting annual layers down from the ice sheet surface. Neither of these methods are feasible for our study, as ice core data are not available everywhere and firn stratigraphy cannot always be assumed to be annual. Instead, we tailor a layer's age to suit MERRA-2's conditions, finding a layer age that will force accumulation rates to converge to MERRA-2 $P - E$ on segment-scale (25 km) by arithmetic mean.

We calculate the age of our single IRH since its original deposition, using the assumption that MERRA-2 $P-E$ is accurate for the 25-km length for which we track this layer. We first derive depth-age profiles for every pick along a 25-km segment using the same MERRA-2-forced firn compaction model described above. Since the depth-age profiles are determined by $P-E$, these profiles do not change within the 25-km segment because a MERRA-2 grid cell is larger than each segment. In reality, the accumulation rates and the depth-age profiles both vary along track, ensuring that the age along the segment remains constant. Instead, the depth-age profiles forced by MERRA-2 are constant, so our calculations result in a range of ages based on our range of depths. Since we assume the layer to be isochronal and intend to force accumulation rates to MERRA-2 $P-E$ on a large scale, we force the mean of this range of estimated ages to equal the MERRA-2-driven layer age.

The quotient of cumulative mass from an IRH to the surface, $CM(x)$, and MERRA-2-driven layer age, age, provides an absolute accumulation rate for each layer pick, x, along each 25-km segment:

$$a_{radar}(x) = \frac{CM(x)}{age}. \quad (1)$$

As in Medley et al. (2015), we refeed this accumulation rate into the firn compaction model to create a new depth-density profile, a new cumulative mass, and a new output accumulation rate. We repeat this process until the output accumulation rate converges with the input accumulation rate (one to two iterations); thus, our cumulative masses and accumulation rates are self-consistent with the depth-density profiles from which they are calculated. This scheme results in very slight changes in along-track accumulation rates (<0.1%).

This process yields an absolute accumulation product in units of meters of water equivalent per year (m w.e. yr^{-1}). This airborne product reflects reanalysis on the scale of a segment (25 km) but resolves 100-m- to 25-km-scale accumulation variability. Since this absolute accumulation product is forced to MERRA-2 $P-E$ on the length scale of a MERRA-2 grid cell, all errors in MERRA-2 $P-E$ are reflected in our absolute accumulation product. For a more detailed analysis of the relationship between our absolute accumulation product and MERRA-2 $P-E$, see supporting information Text S1.

2.2. Relative Radar-Derived Accumulation

Relative accumulation, RA, is the quotient of the pick's cumulative mass, $CM(x)$, and 25-km mean cumulative mass, $\overline{CM}$:

$$RA(x) = \frac{CM(x)}{\overline{CM}}. \quad (2)$$

Relative accumulation is unitless, centered about one, and largely independent of MERRA-2, as relative accumulation is heavily dependent on variations in TWTT along an IRH. For that reason, errors in relative accumulation are found to be very small, with a spatial mean of 0.002 (See supporting information Text S1 for more details).

2.3. Mean Slope in Wind Direction

Mean slope in the (mean) wind direction (MSWD) is defined as the dot product of the topographic surface slope with the annual mean near-surface (10 m) wind direction (Scambos et al., 2012). In this study, topographic surface slopes are derived from the Antarctic CryoSat-2 1-km resolution digital elevation model (DEM; v.1.0) of surface topography (Helm et al., 2014), and wind vector components are based on annual mean (1980–2017) near-surface wind from the MERRA-2 reanalysis that is linearly interpolated onto the DEM grid.

We also quantify the impact of flight direction relative to topography and wind direction on accumulation variability. To do so, we calculate the alignment index, which we define as $|\hat{u} \cdot \hat{f}| * |\hat{s} \cdot \hat{f}|$, where flight direction is $\hat{f}$, topographic slope direction is $\hat{s}$, and wind direction is $\hat{u}$.

3. Results

3.1. Radar-Derived Accumulation Product

On spatial scales exceeding 25 km, our radar-derived absolute accumulation product is forced by MERRA-2 $P-E$, which is shown in Figures 1a and 1b for reference. The spatial distribution of absolute accumulation within MERRA-2 grid cells is illustrated in Figures 1c and 1d. The resolution of absolute accumulation is significantly higher than that of MERRA-2 reanalysis; in the Amundsen Sea Embayment sector, several MERRA-2 grid cells contain over 1,000 radar-derived accumulation measurements each. In addition to its fine-scale resolution, our product represents a wide spatial extent of OIB flight lines over the WAIS and APIS, as demonstrated in Figures 1c through 1l. Regions covered range from coastal zones, where absolute accumulation rates are generally 1.0 m w.e. yr^{-1} or higher, to the high elevation interior around the South Pole, where absolute accumulation rates are 0.03 m w.e. yr^{-1} or lower (Figures 1e and 1f). These absolute accumulation rates reflect MERRA-2 $P-E$ on the length of a MERRA-2 grid cell while representing spatial variations in accumulation on subgrid scales.

In Figures 1g and 1h, our relative accumulation product illustrates these smaller-scale variations with respect to a 25-km binned mean in the along-track direction. To quantify these variations, we calculate

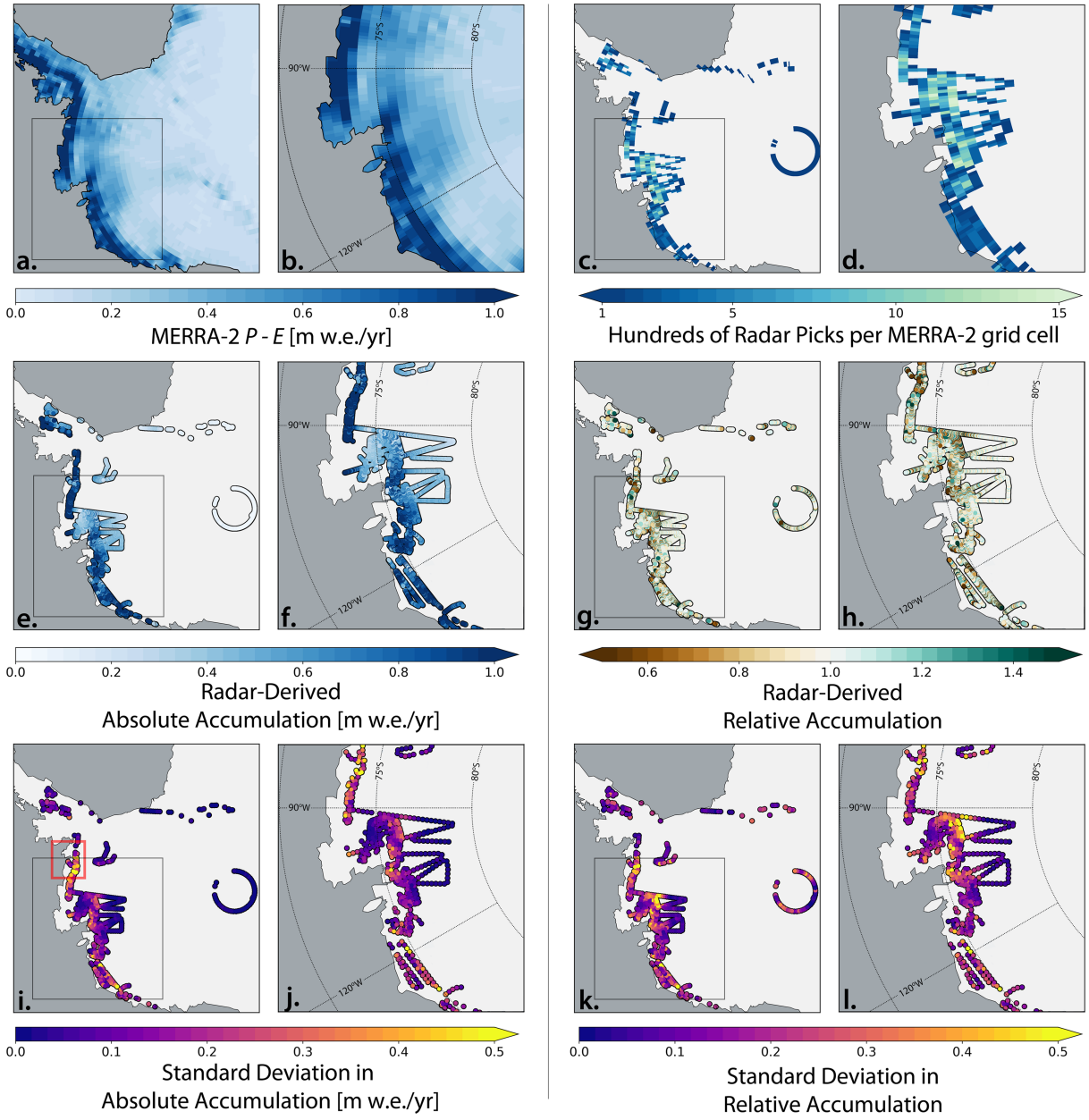

Figure 1. (a, b) Annual mean accumulation rates (m w.e. yr^{-1}) between 1980 and 2017 from MERRA-2 reanalysis. (c, d) Number of accumulation points derived from airborne data per MERRA-2 grid cell. (e, f and g, h) Radar-derived absolute accumulation rates and relative accumulation, respectively. (i, j and k, l) The 25-km standard deviation of radar-derived absolute accumulation rates and relative accumulation, respectively. The second and fourth columns show the same data as the first and third columns, respectively, but centered on the Amundsen Sea Embayment sector, as indicated by the grey boxes in the first and third columns. Red box in (i) outlines the Eights Coast.

standard deviations of accumulation for each 25-km segment. Absolute accumulation rates are highly variable (Figures 1i and 1j) with some regions, such as the Eights Coast, showing standard deviations as high as 0.6 m w.e. yr^{-1}. Standard deviation in relative accumulation reveal variability irrespective of the coast-to-interior gradient in accumulation (Figures 1k and 1l). These standard deviations reach as high as 50% in the Amundsen Sea Embayment sector. The region around the South Pole also shows high spatial accumulation variability, with areas of standard deviations in relative accumulation reaching 40%.

3.2. Relationship Between Wind, Surface Topography, and Accumulation

Our relative accumulation product demonstrates a relationship between accumulation, wind, and surface topography. A 25-km flight segment inland of the Getz Ice Shelf grounding line, shown in Figure 2,

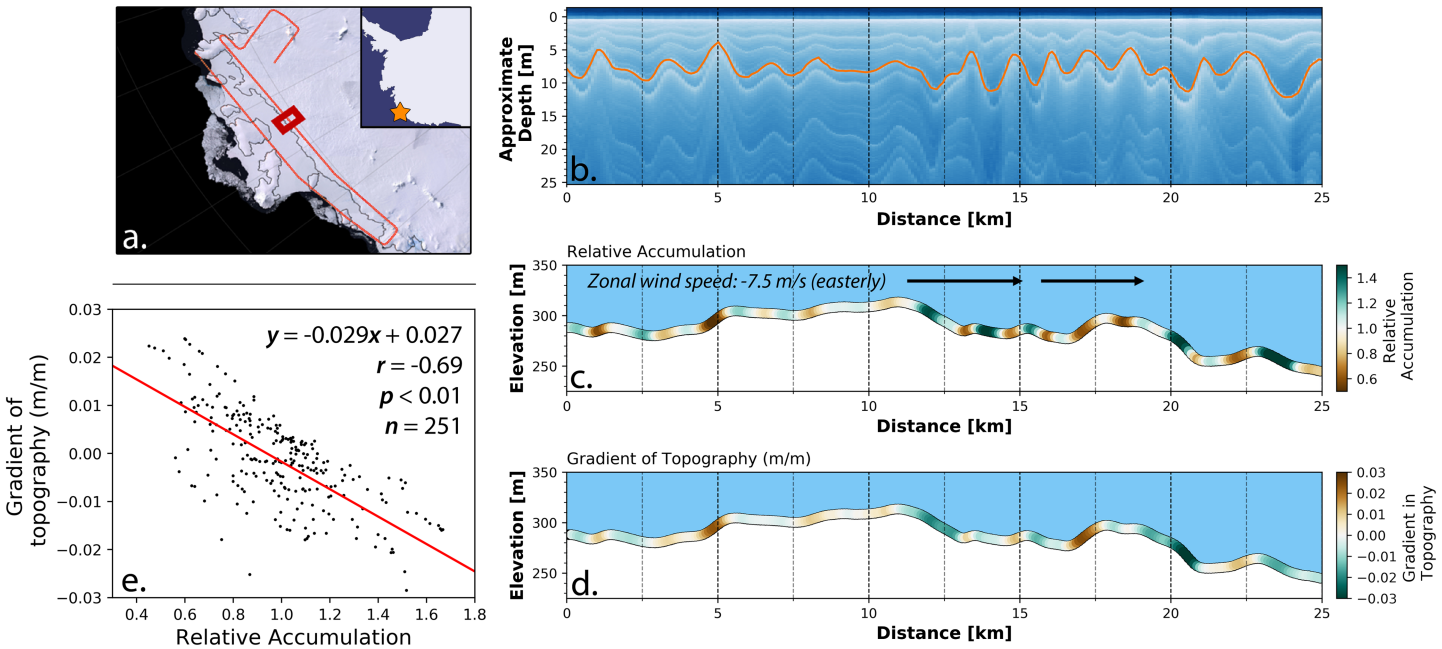

Figure 2. Accumulation, surface topography, and a radar echogram along an OIB flight line close the Getz ice shelf grounding line. (a) Location of the flight line with an orange line and purple box indicating the location of the corresponding flight line and 25-km segment, respectively. An orange star shows the location of this flight line with respect to the WAIS. (b) Snow radar echogram with an orange line indicating the IRH used to compute accumulation rate. (c) Relative accumulation (in line color) following surface elevation from OIB Airborne Topographic Mapper (ATM) along a 25-km flight segment (Studinger, 2014). Wind speed is predominantly easterly and parallel to the flight line, as indicated by the arrows. (d) As (c) but showing gradient in topography. (e) Scatter plot with a linear regression (red line) of gradient of topography (shown in panel d) in flight direction versus relative accumulate rate (shown in panel c).

illustrates this correlation. This flight line was chosen because of the parallel alignment of the near-surface wind and the OIB flight (<10°). The variable depth of the tracked horizon in Figure 2b indicates that accumulation rates are not uniform across this 25-km segment. Relative accumulation rates in Figure 2c reveal this along-track spatial variability. Comparing Figures 2c and 2d, we find that lower accumulation rates colocate with positive topographic surface gradients with respect to wind and higher accumulation rates colocate with negative gradients with respect to wind. Their inverse correlation is shown in Figure 2e ($r = -0.69$;

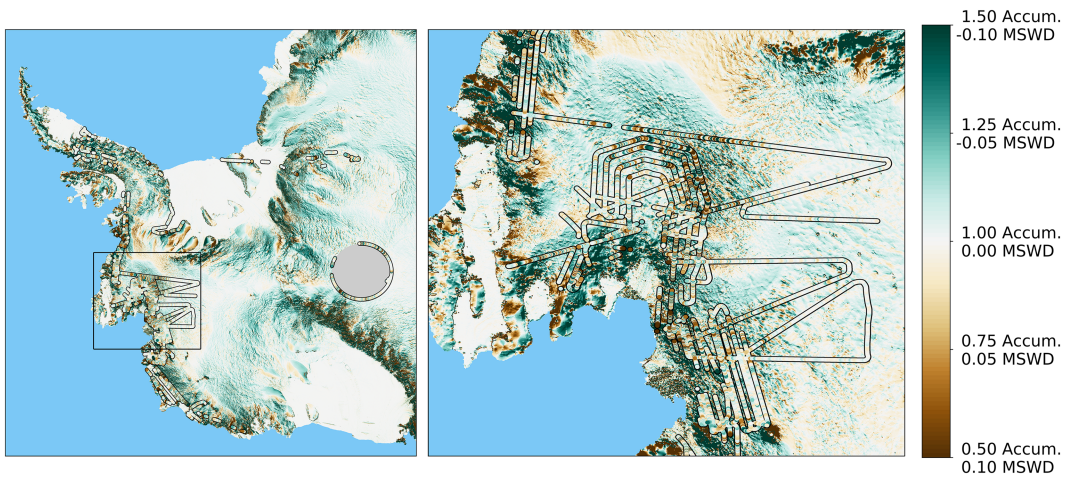

Figure 3. Relative accumulation and MSWD across the WAIS and APIS. Both (a) and (b) show MSWD of the WAIS at a 1-km grid overlaid by relative accumulation with respect to each 25-km segment mean. Brown refers to both low accumulation values and positive MSWD; green refers to high accumulation values and negative MSWD. (b) is focused on the Amundsen Sea Embayment sector (outlined in black in panel a).

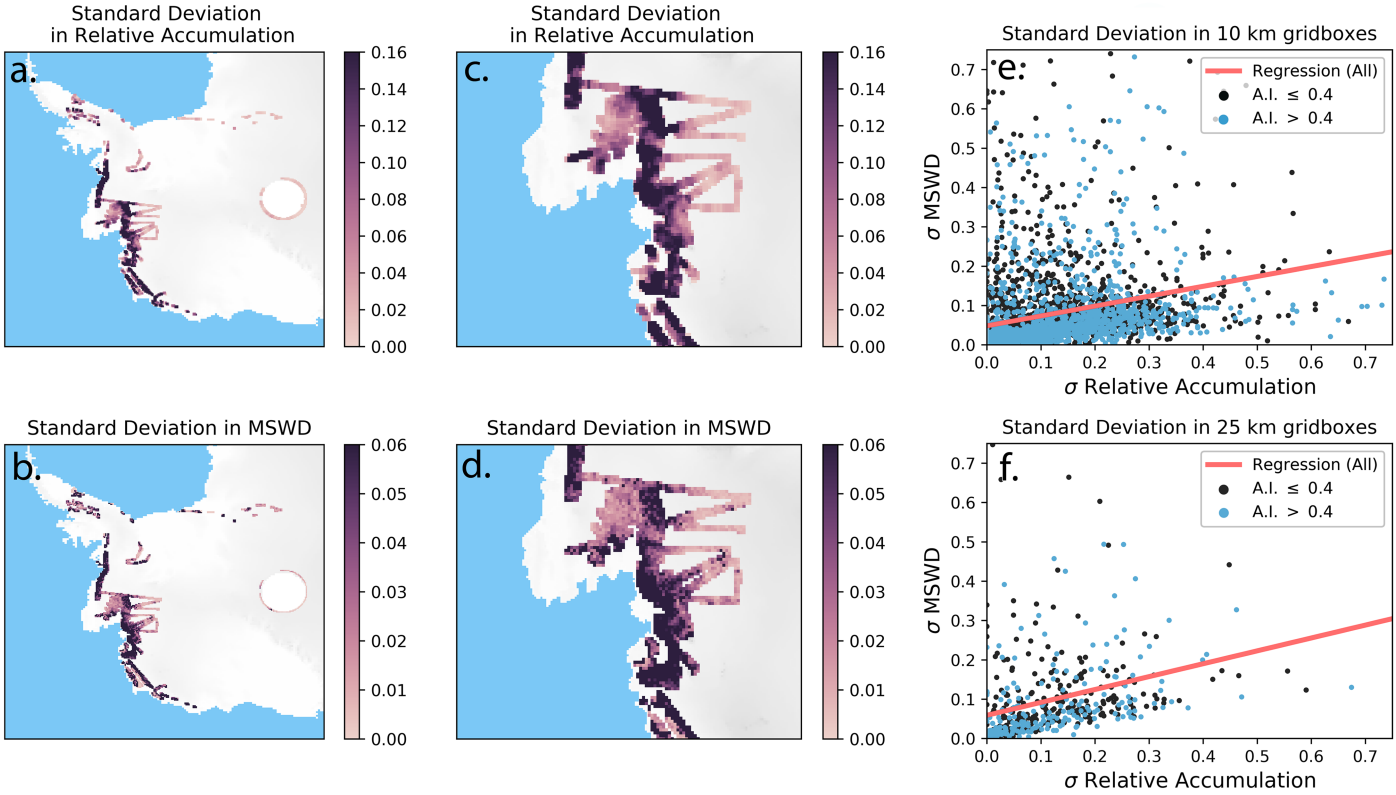

Figure 4. (a and b) Standard deviation within 10-km grid boxes of relative accumulation and MSWD, respectively. (e and f) Standard deviation of MSWD versus standard deviation of relative accumulation rates and their linear regression (red line) within 10- and 25-km grid boxes, respectively.

$p < 0.01$; $n = 251$). Note that all values of p are adjusted for spatial autocorrelation, as detailed in supporting information Table S1. This relationship between wind and topographic surface slope indicates that wind is (1) scouring snow from exposed topography with positive slopes with respect to wind direction and (2) redepositing snow downwind, onto negative slopes with respect to wind direction.

The effects of wind and slope on accumulation can be examined in both horizontal dimensions using gridded MSWD. MSWD, the dot product of wind vectors and topographic surface slopes, is related to small-scale accumulation variability across the ice sheet. In Figures 3a and 3b, high variability in MSWD underlays highly variable accumulation. Likewise, decreased variability in relative accumulation is colocated with near-zero MSWD. Relative accumulation and MSWD do not exhibit a direct correlation with each other, but are related through their spatial patterns in variability.

We quantify this relationship by gridding and comparing standard deviation in MSWD (σ_{MSWD}) to standard deviation in relative accumulation (σ_{RA}) in Figure 4. σ_{MSWD} and σ_{RA} are correlated at a 99% confidence interval with correlation coefficients of 0.21 and 0.28 for grid cell spacings of 10 and 25 km, respectively ($n = 3{,}496$, Figure 4e; $n = 516$, Figure 4f). For alignment indices above 0.4, σ_{MSWD} and σ_{RA} were correlated at or above a 98% confidence interval, with slightly higher correlation coefficients of 0.24 and 0.44 for grid cell spacings of 10 and 25 km, respectively ($n = 1{,}558$, Figure 4e; $n = 232$, Figure 4f). Additionally, extreme values of σ_{MSWD} and σ_{RA} are also related. For both the upper and lower tenth percentiles, σ_{MSWD} and σ_{RA} are colocated at a rate of 85% ± 1%. For more detail about our statistical testing, see supporting information Table S1.

4. Discussion and Conclusions

This study should be regarded as an initial step toward providing a high-resolution, gridded accumulation product over the AIS. We found a relationship between variability in accumulation and surface topography that could be used to inform the downscaling of a reanalysis accumulation product to the grid of a DEM (1 km). Currently, the relationship between relative accumulation and MSWD has limitations. First, we

assumed that the near surface wind climatology in MERRA-2 (0.5° by 0.625°) downscales linearly to a 1 km resolution to compute MSWD. Second, by using a wind climatology to derive MSWD, we ignored seasonality, past variability, and trends in AIS wind climate. However, the near-surface winds on Antarctica (especially in the interior) are predominantly of katabatic nature (Parish & Cassano, 2003), very constant in direction (van den Broeke & van Lipzig, 2003), and forced by downslope surface topography. We therefore assume the AIS near-surface wind field and associated MSWD grid to be relatively persistent and expect little changes in the general AIS wind field in the next decades.

We highlight a few avenues to fine-tune the relationship between MSWD and relative accumulation. MSWD could be recomputed using a new higher resolution (31 km) reanalysis product, European ReAnalysis-5 (ERA-5), if the product is shown to compare better with Antarctic observations than MERRA-2. Furthermore, we could obtain a more accurate MSWD grid by downscaling reanalysis wind fields using an algorithm that modifies wind speed and direction to account for the effects of topography (Liston & Sturm, 1998). Moreover, further refinement of the topography can be obtained using higher-resolution elevation models (Howat et al., 2019; Shean et al., 2016). Additionally, the timing of wind events with respect to surface snow density could be used to modulate MSWD as denser snow is less likely to erode. If a strong inverse correlation between MSWD and relative accumulation is found, a high-resolution gridded (1 km) accumulation product across the AIS could be downscaled from reanalysis based on this relationship.

In our study, we constructed an airborne accumulation product across the WAIS and APIS by using both the snow radar's high along-track resolution and OIB flights' wide spatial coverage. The fine-scale resolution of the instrument allowed us to quantify variability on length scales of 100 m to 25 km. The magnitude of this along-track variability in accumulation rates is nonuniform over the ice sheets. Most notably, high spatial variability of accumulation occurs in the Amundsen Sea Embayment sector, with standard deviation of relative accumulation reaching 50%. Across our data set, we found a significant correlation ($p < 0.01$) between σ_{MSWD} and σ_{RA}. The relationship between extreme values of σ_{MSWD} and σ_{RA} indicates that σ_{MSWD} can be used as a threshold index for σ_{RA}. Overall, our assessment shows that small-scale (<25 km) variations in accumulation are significant, regionally dependent, and driven by wind redistribution of snow.

Acknowledgments
This work is funded by the National Aeronautics and Space Administration (NASA) Studies with ICESat-2 and CryoSat-2 program, Grant 80NSSC18K0201. We thank the CReSIS team for their work developing and maintaining NASA Operation IceBridge's snow radar. We also thank Dr. Alexandra Jahn of University of Colorado Boulder for her input on this paper. Data can be found online (http://doi.org/10.5281/zenodo.3534315).

References

Arcone, S. A., Jacobel, R., & Hamilton, G. (2012). Unconformable stratigraphy in East Antarctica: Part I. Large firn cosets, recrystallized growth, and model evidence for intensified accumulation. *Journal of Glaciology*, *58*(208), 240–252. https://doi.org/10.3189/2012JoJ11J044

Csatho, B., Schenk, A., & Neumann, T. (2019). Ice sheet elevation mapping and change detection with the Ice, Cloud and land Elevation Satellite-2. *International Archives of the Photogrammetry, Remote Sensing and Spatial Information Sciences*, *42*(2/W13), 1747–1751. https://doi.org/10.5194/isprs-archives-XLII-2-W13-1747-2019

Eisen, O., Frezzotti, M., Genthon, C., Isaksson, E., Magand, O., van den Broeke, M. R., et al. (2008). Ground-based measurements of spatial and temporal variability of snow accumulation in East Antarctica. *Reviews of Geophysics*, *46*, RG2001. https://doi.org/10.1029/2006RG000218

Eisen, O., Rack, W., Nixdorf, U., & Wilhelms, F. (2005). Characteristics of accumulation around the EPICA deep-drilling site in Dronning Maud Land, Antarctica. *Annals of Glaciology*, *41*, 41–46. https://doi.org/10.3189/172756405781813276

Fahnestock, M. A., Scambos, T. A., Shuman, C. A., Arthern, R. J., Winebrenner, D. P., & Kwok, R. (2000). Snow megadune fields on the East Antarctic Plateau: Extreme atmosphere-ice interaction. *Geophysical research letters*, *27*(22), 3719–3722. https://doi.org/10.1029/1999GL011248

Frezzotti, M., Gandolfi, S., La Marca, F., & Urbini, S. (2002). Snow dunes and glazed surfaces in Antarctica: New field and remote-sensing data. *Annals of Glaciology*, *34*, 81–88. https://doi.org/10.3189/172756402781817851

Gelaro, R., McCarty, W., Suárez, M. J., Todling, R., Molod, A., Takacs, L., et al. (2017). The Modern-Era Retrospective Analysis for Research and Applications, Version 2 (MERRA-2). *Journal of Climate*, *30*(14), 5419–5454. https://doi.org/10.1175/JCLI-D-16-0758.1

Hawley, R. L., Courville, Z. R., Kehrl, L. M., Lutz, E. R., Osterberg, E. C., Overly, T. B., & Wong, G. J. (2014). Recent accumulation variability in northwest Greenland from ground-penetrating radar and shallow cores along the Greenland inland traverse. *Journal of Glaciology*, *60*(220), 375–382. https://doi.org/10.3189/2014JoG13J141

Helm, V., Humbert, A., & Miller, H. (2014). Elevation and elevation change of Greenland and Antarctica derived from CryoSat-2. *The Cryosphere*, *8*(4), 1539–1559. https://doi.org/10.5194/tc-8-1539-2014

Herron, M. M., & Langway, C. C. (1980). Firn densification: An empirical model. *Journal of Glaciology*, *25*(93), 373–385. https://doi.org/10.3189/S0022143000015239

Howat, I. M., Porter, C., Smith, B. E., Noh, M.-J., & Morin, P. (2019). The reference elevation model of Antarctica. *The Cryosphere*, *13*(2), 665–674. https://doi.org/10.5194/tc-13-665-2019

Kovacs, A., Gow, A. J., & Morey, R. M. (1995). The in-situ dielectric constant of polar firn revisited. *Cold Regions Science and Technology*, *23*(3), 245–256. https://doi.org/10.1016/0165-232X(94)00016-Q

Kuipers Munneke, P., McGrath, D., Medley, B., Luckman, A., Bevan, S., Kulessa, B., et al. (2017). Observationally constrained surface mass balance of Larsen C ice shelf, Antarctica. *The Cryosphere*, *11*, 2411–2426. https://doi.org/10.5194/tc-11-2411-2017

Kuipers Munneke, P., Picard, G., van den Broeke, M., Lenaerts, J., & van Meijgaard, E. (2012). Insignificant change in Antarctic snowmelt volume since 1979. *Geophysical Research Letters*, *39*, L01501. https://doi.org/10.1029/2011GL050207

Lenaerts, J. T. M., van den Broeke, M. R., Déry, S. J., van Meijgaard, E., van de Berg, W. J., Palm, S. P., & Sanz Rodrigo, J. (2012). Modeling drifting snow in Antarctica with a regional climate model: 1. Methods and model evaluation. *Journal of Geophysical Research*, *117*, D05108. https://doi.org/10.1029/2011JD016145

Lenaerts, J. T. M., Ligtenberg, S. R., Medley, B., van de Berg, W. J., Konrad, H., Nicolas, J. P., et al. (2017). Climate and surface mass balance of coastal West Antarctica resolved by regional climate modelling. *Annals of Glaciology*, *59*(76pt1), 29–41. https://doi.org/10.1017/aog.2017.42

Lenaerts, J. T. M., van den Broeke, M. R., van de Berg, W. J., van Meijgaard, E., & Kuipers Munneke, P. (2012). A new, high-resolution surface mass balance map of Antarctica (1979–2010) based on regional atmospheric climate modeling. *Geophysical Research Letters*, *39*, L04501. https://doi.org/10.1029/2011GL050713

Liston, G. E., & Sturm, M. (1998). A snow-transport model for complex terrain. *Journal of Glaciology*, *44*(148), 498–516. https://doi.org/10.3189/S0022143000002021

MacGregor, J. A., Matsuoka, K., Koutnik, M. R., Waddington, E. D., Studinger, M., & Winebrenner, D. P. (2009). Millennially averaged accumulation rates for the Vostok Subglacial Lake region inferred from deep internal layers. *Annals of Glaciology*, *50*(51), 25–34. https://doi.org/10.3189/172756409789097441

Medley, B., Joughin, I., Das, S. B., Steig, E. J., Conway, H., Gogineni, S., et al. (2013). Airborne-radar and ice-core observations of annual snow accumulation over Thwaites Glacier, West Antarctica confirm the spatiotemporal variability of global and regional atmospheric models. *Geophysical Research Letters*, *40*, 3649–3654. https://doi.org/10.1002/grl.50706

Medley, B., Joughin, I., Smith, B. E., Das, S. B., Steig, E. J., Conway, H., et al. (2014). Constraining the recent mass balance of pine island and Thwaites Glaciers, West Antarctica, with airborne observations of snow accumulation. *The Cryosphere*, *8*(4), 1375–1392. https://doi.org/10.5194/tc-8-1375-2014

Medley, B., Ligtenberg, S. R. M., Joughin, I., van den Broeke, M. R., Gogineni, S., & Nowicki, S. (2015). Antarctic firn compaction rates from repeat-track airborne radar data: I. Methods. *Annals of Glaciology*, *56*(70), 155–166. https://doi.org/10.3189/2015AoG70A203

Medley, B., & Thomas, E. R. (2019). Increased snowfall over the Antarctic Ice Sheet mitigated twentieth-century sea-level rise. *Nature Climate Change*, *9*(1), 34. https://doi.org/10.1038/s41558-018-0356-x

Nicolas, J. P., & Bromwich, D. H. (2011). Climate of West Antarctica and influence of marine air intrusions. *Journal of Climate*, *24*(1), 49–67. https://doi.org/10.1175/2010JCLI3522.1

Palerme, C., Genthon, C., Claud, C., Kay, J. E., Wood, N. B., & L'Ecuyer, T. (2017). Evaluation of current and projected Antarctic precipitation in CMIP5 models. *Climate Dynamics*, *48*(1-2), 225–239. http://doi.org/10.1007/s00382-016-3071-1

Parish, T. R., & Cassano, J. J. (2003). The role of katabatic winds on the Antarctic surface wind regime. *Monthly Weather Review*, *131*(2), 317–333. https://doi.org/10.1175/1520-0493(2003)131%3C0317:TROKWO%3E2.0.CO;2

Rignot, E., Mouginot, J., Scheuchl, B., van den Broeke, M., van Wessem, M. J., & Morlighem, M. (2019). Four decades of Antarctic Ice Sheet mass balance from 1979–2017. *Proceedings of the National Academy of Sciences*, *116*(4), 1095–1103. https://doi.org/10.1073/pnas.1812883116

Sandberg Sørensen, L., Simonsen, S. B., Nielsen, K., Lucas-Picher, P., Spada, G., Adalgeirsdottir, G., et al. (2011). Mass balance of the Greenland ice sheet (2003–2008) from ICESat data? The impact of interpolation, sampling and firn density. *The Cryosphere*, *5*, 173–186. https://doi.org/10.5194/tc-5-173-2011

Scambos, T. A., Frezzotti, M., Haran, T., Bohlander, J., Lenaerts, J. T. M., van den Broeke, M. R., et al. (2012). Extent of low-accumulation 'wind glaze' areas on the East Antarctic Plateau: Implications for continental ice mass balance. *Journal of Glaciology*, *58*(210), 633–647. https://doi.org/10.3189/2012JoG11J232

Shean, D. E., Alexandrov, O., Moratto, Z. M., Smith, B. E., Joughin, I. R., Porter, C., & Morin, P. (2016). An automated, open-source pipeline for mass production of digital elevation models (DEMs) from very-high-resolution commercial stereo satellite imagery. *ISPRS Journal of Photogrammetry and Remote Sensing*, *116*, 101–117. https://doi.org/10.1016/j.isprsjprs.2016.03.012

Shepherd, A., Ivins, E., Rignot, E., Smith, B., van den Broeke, M., Velicogna, I., et al. (2018). Mass balance of the Antarctic Ice Sheet from 1992 to 2017. *Nature*, *558*, 219–222. https://doi.org/10.1038/s41586-018-0179-y

Sinisalo, A., Grinsted, A., Moore, J. C., Kärkäs, E., & Pettersson, R. (2003). Snow-accumulation studies in Antarctica with ground-penetrating radar using 50, 100 and 800 mHz antenna frequencies. *Annals of Glaciology*, *37*, 194–198. https://doi.org/10.3189/172756403781815825

Studinger, M. 2014, updated 2018. IceBridge ATM L2 Icessn Elevation, Slope, and Roughness, Version 2. Boulder, Colorado USA: NASA National Snow and Ice Data Center Distributed Active Archive Center. https://doi.org/10.5067/CPRXXK3F39RV. Accessed November 2018.

Trusel, L. D., Frey, K. E., Das, S. B., Munneke, P. K., & van den Broeke, M. R. (2013). Satellite-based estimates of Antarctic surface meltwater fluxes. *Geophysical Research Letters*, *40*, 6148–6153. https://doi.org/10.1002/2013GL058138

van den Broeke, M., & van Lipzig, N. (2003). Factors controlling the near-surface wind field in Antarctica. *Monthly Weather Review*, *131*(4), 733–743. https://doi.org/10.1175/1520-0493(2003)131%3C0733:FCTNSW%3E2.0.CO;2

van den Broeke, M., van de Berg, W. J., & van Meijgaard, E. (2006). Snowfall in coastal West Antarctica much greater than previously assumed. *Geophysical Research Letters*, *33*, L02505. https://doi.org/10.1029/2005GL025239

Zwally, H. J., Li, J., Robbins, J. W., Saba, J. L., Yi, D., & Brenner, A. C. (2015). Mass gains of the Antarctic Ice Sheet exceed losses. *Journal of Glaciology*, *61*(230), 1019–1036. https://doi.org/10.3189/2015JoG15J071